J. Fluid Mech. (2012), *vol.* 699, *pp.* 153–173. © Cambridge University Press 2012
doi:10.1017/jfm.2012.90

Spontaneous inertia-gravity-wave generation by surface-intensified turbulence

E. Danioux[1]†, J. Vanneste[1], P. Klein[2] and H. Sasaki[3]

[1] School of Mathematics and Maxwell Institute for Mathematical Sciences, University of Edinburgh, King's Buildings, Edinburgh EH9 3JZ, UK

[2] Laboratoire de Physique des Océans, Ifremer-CNRS-UBO-IRD, 29280 Plouzané, France

[3] Earth Simulator Center, JAMSTEC, 3173-25 Showa-machi, Kanazawa-ku, Yokohama, Kanagawa 236-0001, Japan

(Received 30 March 2011; revised 22 November 2011; accepted 14 February 2012; first published online 24 April 2012)

The spontaneous generation of inertia-gravity waves (IGWs) by surface-intensified, nearly balanced motion is examined using a high-resolution simulation of the primitive equations in an idealized oceanic configuration. At large scale and mesoscale, the dynamics, which is driven by baroclinic instability near the surface, is balanced and qualitatively well described by the surface quasi-geostrophic model. This however predicts an increase of the Rossby number with decreasing spatial scales and, hence, a breakdown of balance at small scale; the generation of IGWs is a consequence of this breakdown. The wave field is analysed away from the surface, at depths where the associated vertical velocities are of the same order as those associated with the balanced motion. Quasi-geostrophic relations, the omega equation in particular, prove sufficient to separate the IGWs from the balanced contribution to the motion. A spectral analysis indicates that the wave energy is localized around dispersion relation for free IGWs, and decays only slowly as the frequency and horizontal wavenumber increase. The IGW generation is highly intermittent in time and space: localized wavepackets are emitted when thin filaments in the surface density are formed by straining, leading to large vertical vorticity and correspondingly large Rossby numbers. At depth, the IGW field is the result of a number of generation events; away from the generation sites it takes the form of a relatively homogeneous, apparently random wave field. The energy of the IGW field generated spontaneously is estimated and found to be several orders of magnitude smaller than the typical IGW energy in the ocean.

Key words: internal waves, quasi-geostrophic flows, wave–turbulence interactions

1. Introduction

A fundamental feature of geophysical fluid dynamics, relevant to both the atmosphere and ocean, is the separation between balanced motion and inertia-gravity waves (IGWs). In many regions, the two types of motion are well separated, with the slow, balanced motion largely unaffected by the much faster IGWs. This separation, which stems from the large frequency gap between the two types of motion and is estimated by the (small) Rossby number, is well understood. The separation is

† Present address: Northwest Research Associates, Bellevue, WA 98009-3027, USA. Email address for correspondence: edanioux@gmail.com

https://doi.org/10.1017/jfm.2012.90 Published online by Cambridge University Press

not complete, however; as a result, balanced motion constantly leaks some energy to IGWs, thus providing a source of IGW generation through the mechanism known as spontaneous generation. This mechanism is of interest in particular because it potentially excites IGWs across the whole spectrum of wavelengths and frequencies. This contrasts with other sources, such as tidal and wind forcing in the ocean, or topographic and convective forcing in the atmosphere, which have a determined frequency.

In recent years, spontaneous generation has been demonstrated in a number of numerical simulations (e.g. O'Sullivan & Dunkerton 1995; Zhang 2004; Viudez & Dritschel 2006; Plougonven & Snyder 2005, 2007; Snyder *et al.* 2007) and in idealized models (e.g. Vanneste & Yavneh 2004; Ólafsdóttir, Olde Daalhuis & Vanneste 2008). Theoretical arguments suggest that this generation is exceedingly small when the Rossby number is small: exponentially so, as asymptotic results indicate (Vanneste 2008*b*, and references therein). Non-negligible IGW generation is therefore expected only in regions where the Rossby number is of order one or larger. In the absence of direct external forcing, large Rossby numbers typically do not emerge in the interior of geophysical fluids: flows that are balanced initially remain so. This is true even in the presence of turbulence because the steep energy spectra of the (forward, enstrophy) cascade of balanced turbulence is associated with Rossby numbers that are essentially scale-independent. However, the situation changes radically when horizontal boundaries such as the ocean or Earth's surface, or the tropopause are taken into account. In this case, the evolution of the surface (potential) temperature which, together with the interior potential vorticity, controls the balanced dynamics, leads to shallow energy spectra, vorticity intensification and hence large local Rossby numbers at the surface. This is most easily demonstrated using the surface-quasi-geostrophic (SQG) model (e.g. Held *et al.* 1995). Indeed simple scaling arguments based on the surface energy spectrum $E(k_h) \sim k_h^{-5/3}$ predicted in SQG suggest that the Rossby number scales with the horizontal wavenumber as $Ro \sim k_h^{2/3}$ (see Blumen 1978; Juckes 1994, (7.14)), so that large Rossby numbers always appear at small enough horizontal scales in near-surface flows even though they are balanced at large scales. Therefore, as Juckes (1994) argues, balance breaks down at some stage. IGW generation can be expected at some point in this process.

These scaling arguments are substantiated by process studies which have identified frontogenesis as a mechanism for IGW generation by surface-intensified flows. The classical two-dimensional models of frontogenesis driven by vertical shear (Williams 1967) or horizontal strain (Hoskins & Bretherton 1972), which in the semi-geostrophic approximation predict a finite-time singularity, have been examined using two-dimensional primitive-equation simulations (Snyder, Skamarock & Rotunno 1993; Griffiths & Reeder 1996; Reeder & Griffiths 1996, and references therein). These studies demonstrate that the breakdown of the (semi-geostrophic) balance in these flows is accompanied by the emission of IGWs whose amplitudes depend strongly on the speed of the frontogenesis evolution. This mechanism has also been found in three-dimensional simulations of baroclinic instability where surface fronts develop (Zhang 2004; Plougonven & Snyder 2007).

While most of the work on the breakdown of balance near horizontal boundaries was motivated by applications to the atmosphere, the importance of near-surface, SQG-like motion in the ocean is increasingly recognized (e.g. Lapeyre & Klein 2006). In particular, the formation of fronts that characterize surface motion, and their subsequent instability in regimes far from geostrophy have been identified as

https://doi.org/10.1017/jfm.2012.90 Published online by Cambridge University Press

sources of submesoscale motion (Capet *et al.* 2008*a*,*b*,*c*; McWilliams, Molemaker & Ólafsdóttir 2009), along with possible implications for the energy balance in the ocean (Molemaker, McWilliams & Capet 2010).

In the present paper, we also consider the oceanic context, but with a different focus which concentrates on IGW generation. The main aim is to demonstrate that the argument put forward by Juckes (1994) applies to the ocean and that IGWs are generated spontaneously by what can be described in the first approximation as SQG turbulence. While the generation process involved is similar to the frontal emission of Snyder *et al.* (1993) and Griffiths & Reeder (1996), our focus is on the global behaviour of a complex, turbulent, three-dimensional flow as a wave emitter rather than on single wave emission events. We pay particular attention to the spectral characteristics of the IGW field. Specifically, we analyse a high-resolution simulation of an ocean jet driven by baroclinic instability into a regime of statistically steady, surface-intensified turbulence, and examine how this turbulence spontaneously radiates IGWs which propagate into the ocean's interior. The IGW signal is weak compared with the balanced signal and best inferred at depth since the balanced signal decays with depth (exponentially so in SQG). We use diagnostic tools based on quasi-geostrophic theory, the omega equation in particular, in order to separate IGWs and balanced motion. The analysis shows that spontaneous generation is highly intermittent both in space and time: wavepackets are produced by a number of generation events which we associate with the formation of thin filaments of surface density (here equivalent to potential temperature), with strong vertical vorticity, which is produced by straining. Although the emission of inertia-gravity wavepackets is highly intermittent, their subsequent propagation and dispersion leads to what appears as a random, almost homogeneous IGW field at depth. A spectral analysis of this field confirms that it consists of free IGWs obeying the dispersion relation. Our results support the argument that the cascade to small-scale inherent to surface motion leads to balance breakdown and IGWs generation. However, an estimation of the energy associated with these spontaneously emitted waves indicates that it is orders of magnitude smaller than the typical energy for (wind and tidally driven) internal waves.

The plan of the paper is as follows. We briefly describe the numerical model used and the set-up of the simulation in § 2. Section 3 is devoted to the diagnostic tools necessary to separate IGWs from the balanced motion. These use the omega equation and another quasi-geostrophic balance relation, together with a specific energy-minimizing projection. The IGW field obtained in the simulation is analysed in § 4. We first examine the physical and spectral characteristics of the entire wave field, estimate its energy, before describing a typical wave-generation event. The paper concludes with a discussion in § 5.

2. Model set-up

We analyse a high-resolution simulation of ocean turbulence modelled by the primitive equations under the Boussinesq and hydrostatic approximations. The numerical model and parameter set-up employed for this simulation are similar to those in Klein *et al.* (2008). We describe them briefly and refer the reader to this paper for more detail.

The numerical model (the Regional Oceanic Modeling System (ROMS), Shchepetkin & McWilliams 2005) is a σ-coordinate model used in a periodic channel configuration, with free-slip boundary conditions at northern and southern walls. The domain size is 500 km $\times$ 2000 km in the horizontal, with a depth of 4 km. The

https://doi.org/10.1017/jfm.2012.90 Published online by Cambridge University Press

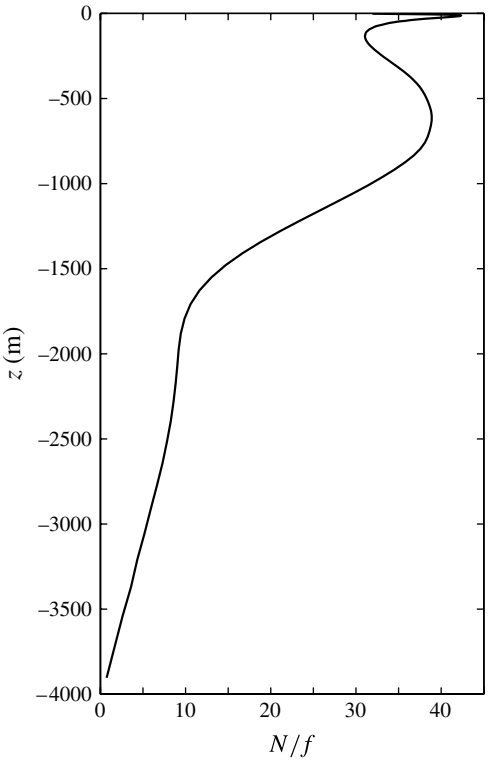


FIGURE 1. Horizontally averaged profile of the ratio of the Brunt–Väisälä frequency to the Coriolis frequency in the simulation.

numerical resolution is 2 km × 2 km in the horizontal and 100 levels in the vertical (the vertical grid spacing ranges from 3 m near the surface to 200 m near the bottom). Vertical mixing in the interior is represented by a K-profile parameterization (KPP, Large, Doney & McWilliams 1994). The numerical dissipation of the model is sufficient for stability without resorting to explicit viscous damping. Salinity is taken as constant, so that temperature anomalies are proportional to density anomalies. There is no atmospheric forcing.

An energetic turbulent mesoscale and submesoscale eddy field is generated through the baroclinic instability of a balanced, surface-intensified, westerly zonal flow centred in the middle of the channel. The parameter settings for this flow resemble those used by Karsten, Jones & Marshall (2002), Rivière, Tréguier & Klein (2004) and Lapeyre & Klein (2006). The initial vertical profile of the mean Brunt–Väisälä frequency (figure 1) represents a main thermocline located at a depth of around 600 m, corresponding to a first Rossby radius of deformation of approximately 25 km. No surface mixed layer is initially present. The zonal flow is maintained throughout the simulation using a relaxation of the zonally averaged velocity and density fields to the initial state. The relaxation time is chosen as 50 days. While maintaining the zonal-mean flow, this forcing does not damp the eddies, leading to a vigorous turbulent eddy field.

After a spinup of 350 days, the total kinetic energy (integrated over the whole domain) has saturated, and a statistically steady state is reached. The results described

https://doi.org/10.1017/jfm.2012.90 Published online by Cambridge University Press

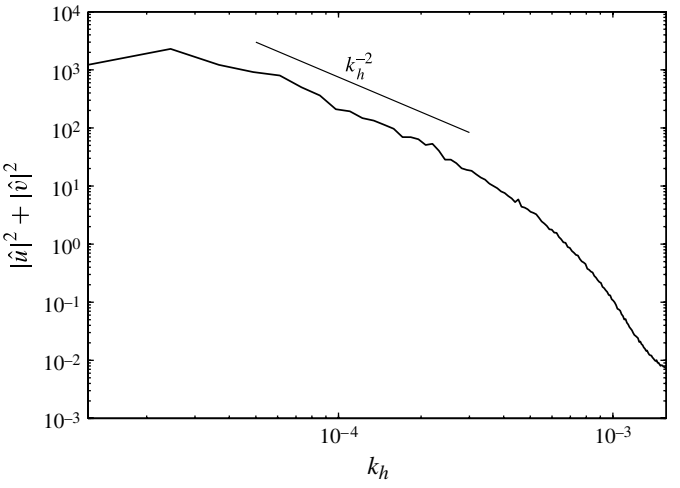


FIGURE 2. Horizontal wavenumber spectrum of the surface kinetic energy.

in this paper concern the flow well after this spinup period. The surface energy spectrum, shown in figure 2, approximately displays a k_h^{-2} dependence for length scales ranging from 20 to 130 km, and a k_h^{-3} dependence for length scales ranging from 10 to 20 km. This k_h^{-2} spectrum is substantially steeper than the SQG prediction $E(k_h) \sim k_h^{-5/3}$, but in agreement with the results of Lapeyre & Klein (2006). We refer the reader to that paper for a detailed discussion of the applicability and limitations of SQG as a model of the near-surface flow. From our viewpoint, what is important is that this steeper spectrum does not invalidate the argument about Rossby numbers increasing with k_h mentioned in § 1: using the frequency estimate $\omega \sim (\int^{k_h} k'^2 E(k')\,\mathrm{d}k')^{1/2}$ (Kraichnan 1971) with $E(k_h) \sim k_h^{-2}$ yields $Ro \sim \omega/f \sim k_h^{1/2}$.

The surface vorticity typically varies between $-f$ and $4f$, where f is the Coriolis frequency. These large values, which arise locally from the straining of small-scale density filaments, are associated with the generation of IGWs. The asymmetry between cyclonic and anticyclonic vorticity is marked; as a result, IGW generation is largely limited to cyclonic flow features. Note that while the mesoscale field obtained is strongly energetic, there is substantially less activity at the smallest scales than in the simulations of Capet *et al.* (2008*b*) and in particular no evidence of submesoscale instabilities, presumably as a result of our lower horizontal resolution (2 km versus 750 m) and larger numerical viscosity.

3. Balanced motion and IGWs

Our aim is to examine the IGWs that are generated spontaneously by the near-surface, balanced turbulence and propagate into the deep ocean. The distinction between balanced motion and IGWs, or more generally unbalanced motion, is clear in the limit of small Rossby number $Ro \ll 1$. In this limit, it is possible to define balance relations which relate all dynamical variables to a single one, often potential vorticity. Geometrically, this is often thought of as the definition of slow manifolds which are approximately invariant: nearly balanced motion evolves in the neighbourhood of these manifolds but slowly drifts away as a result of spontaneous generation of IGWs. Balanced relations are most easily constructed systematically using asymptotic

https://doi.org/10.1017/jfm.2012.90 Published online by Cambridge University Press

series expansions in powers of Ro; this leads to a hierarchy of relations of increasing accuracy, starting with geostrophic balance (Warn *et al.* 1995; Vanneste 2008*b*). Unless the asymptotic expansions are carried out to optimal truncation, the separation between balanced and unbalanced motion is always ambiguous: the difference between the full dynamical fields and those of the corresponding balanced state obtained by projection on a slow manifold results from the limited accuracy of the balance relation used as well as from the presence of genuine unbalanced motion.

In what follows, we will only use the leading-order, geostrophic balance. This is sufficient for our purpose because we concentrate on the fields at depth: in qualitative agreement with SQG theory, the intensity of the turbulence in the flow analysed decays rapidly with depth while its typical horizontal scales increase. This leads to Rossby numbers at depth that are much smaller than at the surface; for instance, using the ratio of relative to planetary vorticity gives on average $Ro < 0.06$ at 2500 m. In addition, the characteristics of the unbalanced motion away from the region of generation are different from those of the balanced motion. They consist of small-scale IGWs with a clear wavenumber–frequency signature. We now discuss the methods that we use to extract this IGW signal using the geostrophic balance relation.

3.1. *Vertical velocity*

Let us consider the separation of the dynamical fields between a geostrophic, a balanced ageostrophic and unbalanced contribution. By balanced ageostrophic, we mean the corrections to geostrophic balance that are obtained using higher-order balance relations which slave all of the fields to a single one, say the potential vorticity. As mentioned above, these relations can be obtained systematically using asymptotic expansions in powers of the Rossby number (Warn *et al.* 1995); since they diverge, the expansions must be truncated; conceptually (if not practically), it is useful to think of the truncation as being an optimal one, near the smallest term (Bender & Orszag 1999), so that the remainder is dominated by unbalanced motion (Vanneste 2008*a*,*b*; Temam & Wirosoetisno 2011).

The decomposition of the horizontal and vertical non-dimensionalized velocities gives terms of the following orders of magnitudes:

$$u = \underbrace{u_g}_{O(1)} + \underbrace{u_{bag}}_{O(Ro)} + \underbrace{u_{unb}}_{O(\alpha)} \quad \text{and} \quad w = \underbrace{w_{bag}}_{O(Ro)} + \underbrace{w_{unb}}_{O(\alpha)}, \tag{3.1}$$

where α is the amplitude of the unbalanced motion which we aim to determine. Most fields, the density in particular, obey a scaling comparable to that of the horizontal velocity u. This makes it clear that the vertical velocity w is better suited for the identification of IGWs than these other fields (the divergence of the horizontal velocity field is similar in this respect). The analysis below suggests that α and Ro have comparable orders of magnitude in the bottom half of our simulation, so that the unbalanced part of w can be detected in the total field. Note, however, that this is based on a local Ro whereas the validity of balance relations, which involve non-local operators, in principle requires that Ro be uniformly small, an assumption that is clearly not satisfied in the flow we consider.

Although IGWs can be identified in the total vertical velocity w, mainly thanks to their distinctive spatial structure (see § 4), it is useful to use a balance relation in order to diagnose w_{bag} and better isolate the IGW contribution w_{unb}. This relation is provided

https://doi.org/10.1017/jfm.2012.90 Published online by Cambridge University Press

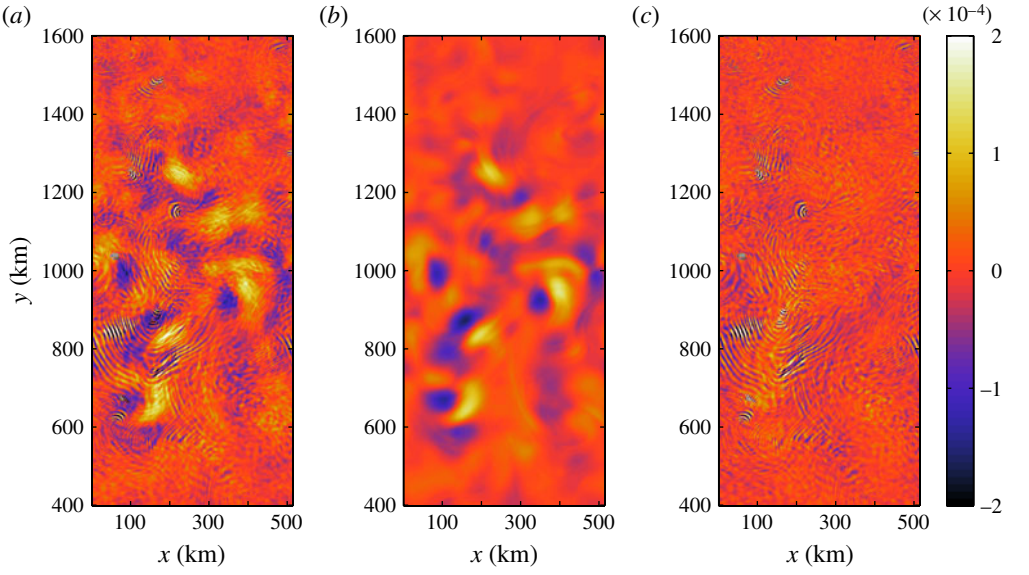


FIGURE 3. (Colour online available at journals.cambridge.org/flm) Vertical velocity (in m s^{-1}) at $z = -2500$ m: (*a*) total velocity w; (*b*) quasi-geostrophic approximation w_{qg} obtained by solving the omega equation; (*c*) unbalanced contribution $w_{unb} = w - w_{qg}$. Note that absolute values larger than 2×10^{-4} m s^{-1} may occur locally.

by the quasi-geostrophic omega equation (Hoskins, Draghici & Davies 1978)

$$\nabla_h^2 w_{qg} + \frac{f^2}{N^2}\frac{\partial^2 w_{qg}}{\partial z^2} = \frac{2g}{\rho_0 N^2}\nabla_h \cdot \boldsymbol{Q}, \tag{3.2}$$

where $\nabla_h = (\partial_x, \partial_y)$ denotes the horizontal gradient, and

$$\boldsymbol{Q} = (\nabla_h \boldsymbol{u}_h)^{\mathrm{T}} \cdot \nabla_h \rho, \tag{3.3}$$

with $\boldsymbol{u}_h = (u, v)$ the horizontal velocity. Equation (3.2) is solved with the boundary conditions $w_{qg}(z = 0) = w_{qg}(z = -H) = 0$. The geostrophic approximation to the vertical velocity that is obtained, w_{qg}, is the leading order of w_{bag}: $w_{bag} = w_{qg} + O(Ro^2)$. Note that, in quasi-geostrophic theory, $\boldsymbol{Q}$ is defined in terms of the geostrophic approximation to $\boldsymbol{u}_h$ and ρ; instead, we use the full fields since this provide an estimate of w_{bag} with the same formal accuracy. The use of the quasi-geostrophic omega equation (3.2), compared with more sophisticated balance relations (e.g. Muraki, Snyder & Rotunno 1999) or approaches taking into account dissipation in the surface mixed layer (Nagai, Tandon & Rudnick 2006), is justified *a posteriori* by the efficiency of our method (see figures 3 and 4).

For the results reported in § 4, we solve (3.2) on the ROMS grid using the free-access mudpack solver (multigrid software for elliptic partial differential equations, see Adams (1989)). Once w_{qg} is obtained, the difference $w - w_{qg} = w_{unb} + O(Ro^2)$ gives an estimate for the IGW contribution to the vertical velocity.

3.2. *Horizontal velocity*

For comparison, it is also useful to estimate the IGW contribution to dynamical fields other than w. If a geostrophic approximation is computed, say for the zonal velocity u,

https://doi.org/10.1017/jfm.2012.90 Published online by Cambridge University Press

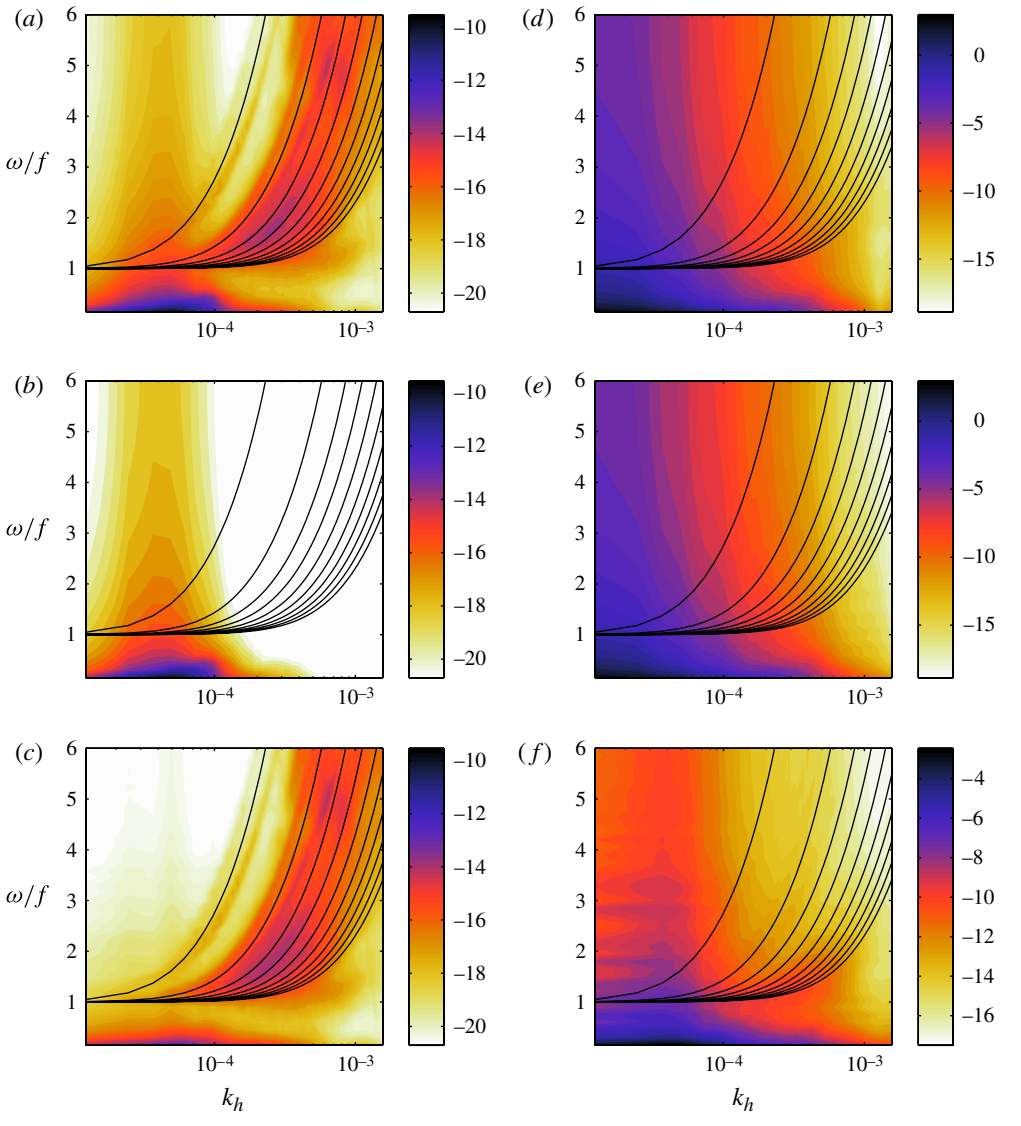


FIGURE 4. (Colour online) Frequency–horizontal wavenumber spectrum (log-scale) at $z = -2500$ m. (*a–c*) Vertical velocity, w (*a*), w_{qg} (*b*) and w_{unb} (*c*). (*d–f*) Horizontal kinetic energy, total (*d*), quasi-geostrophic (*e*) and unbalanced (*f*). The dispersion relation $\omega^2 = f^2 + f^2 r_n^2 k_h^2$ for the first 10 vertical modes is indicated by black curves. Note that the colourbar of (*f*) differs from that of (*d*,*e*).

then the IGWs may be identifiable by considering $u - u_g = u_{unb} + O(Ro)$. The diagnostic of balanced fields from data raises an issue which appears to be often overlooked, the need for a projection: a balance relation, geostrophy in our case, defines a slow manifold, but it does not give a unique means of projecting arbitrary data on this slow manifold.

A possible projection consists in insisting that the potential vorticity be the same in the unprojected state (off the slow manifold) and the projected state (on the slow

https://doi.org/10.1017/jfm.2012.90 Published online by Cambridge University Press

manifold). This particular projection does not have a strong motivation, and it does not necessarily make obvious which potential vorticity (Rossby–Ertel, quasi-geostrophic, linearized) should be chosen. Here we adopt a somewhat different approach: for given velocity and density fields $\boldsymbol{u}$ and ρ, we seek the nearest geostrophic state

$$(\boldsymbol{u}_g, \rho_g) = \left(\boldsymbol{\nabla}_h^{\perp} \psi, -\frac{\rho_0 f}{g} \frac{\partial \psi}{\partial z} \right) \quad \text{with } \boldsymbol{\nabla}_h^{\perp} = (-\partial_y, \partial_x), \tag{3.4}$$

where 'nearest' is understood in the sense of some norm. The choice of norm is arbitrary; we choose a norm based on the average energy per unit volume

$$\mathscr{E} = \frac{\rho_0}{2V} \iiint \left[u^2 + v^2 + \left(\frac{g\rho}{N\rho_0} \right)^2 \right] \mathrm{d}x\, \mathrm{d}y\, \mathrm{d}z, \tag{3.5}$$

where V is the domain volume, which is conserved for the primitive equations in the absence of forcing and dissipation and for suitable boundary conditions (e.g. no normal velocity). Specifically, we project any state on the geostrophic state (3.4) by finding the streamfunction ψ which achieves

$$\min_{\psi} \left(\frac{\rho_0}{2V} \iiint \left[|\boldsymbol{u} - \boldsymbol{u}_g|^2 + \left(\frac{g}{N\rho_0} \right)^2 (\rho - \rho_g)^2 \right] \mathrm{d}x\, \mathrm{d}y\, \mathrm{d}z \right). \tag{3.6}$$

For the boundary conditions $\rho_g = \rho$ at $z = 0, -H$ and $\boldsymbol{u}_g = \boldsymbol{u}_h$ on the lateral boundaries, a simple variational calculation shows that this minimum is reached when ψ solves the equation

$$\nabla_h^2 \psi + \frac{\partial}{\partial z} \left(\frac{f^2}{N^2} \frac{\partial \psi}{\partial z} \right) = \hat{\boldsymbol{z}} \cdot (\boldsymbol{\nabla}_h \times \boldsymbol{u}_h) - \frac{gf}{\rho_0} \frac{\partial}{\partial z} \left(\frac{\rho}{N^2} \right), \tag{3.7}$$

where $\hat{\boldsymbol{z}}$ denotes a vertical unit vector.

The left-hand side of (3.7) is the usual quasi-geostrophic potential vorticity, a quantity that is conserved by the advection in the quasi-geostrophic approximation. The right-hand side is neither the total potential vorticity nor the linearized vorticity divided by N^2 (in both cases the factor N^{-2} would be undifferentiated); rather it resembles the quasi-geostrophic potential vorticity, with the total velocity and density replacing their quasi-geostrophic approximations $\boldsymbol{\nabla}^{\perp}\psi$ and $-f\rho_0 \partial_z \psi / g$, respectively. We solve (3.7), similarly to (3.2), on the ROMS grid using the mudpack solver.

3.3. *IGW energy*

The discussion above indicates that for a similar computational effort (the solution of a three-dimensional linear elliptic equation) we can obtain either the sum $w_{unb} + O(Ro^2)$ or the sum $\boldsymbol{u}_{unb} + O(Ro)$, where the error terms consist of the balanced part of the flow not captured by geostrophic balance. It is clear, therefore, that it is advantageous to express quantities such as the unbalanced energy in terms of w alone when possible.

One way to do so is to project the dynamical fields on suitable vertical normal modes and exploit results of linear wave theory, namely the IGW dispersion and polarization relations, to relate all dynamical fields to the projection of w.

Let us define the functions F_n as eigenfunctions of the Sturm–Liouville problem

$$\partial_z \left(\frac{f^2}{N^2} \partial_z F_n \right) = -\frac{1}{r_n^2} F_n, \quad \partial_z F_n = 0 \quad \text{at } z = 0, -H, \tag{3.8}$$

https://doi.org/10.1017/jfm.2012.90 Published online by Cambridge University Press

where the deformation radii r_n are the eigenvalues (e.g. Gill 1982). We define the additional functions G_n and H_n by

$$G_n(z) = r_n f \partial_z F_n, \quad H_n(z) = \int_z^0 F_n(z')\,\mathrm{d}z' \tag{3.9}$$

(see Danioux & Klein 2008 and Danioux, Klein & Rivière 2008). It is easy to verify that these functions are orthogonal in the sense that

$$\int_{-H}^0 F_n F_m\,\mathrm{d}z = \delta_{m,n}, \quad \int_{-H}^0 N^{-2} G_n G_m\,\mathrm{d}z = \delta_{m,n}, \quad \int_{-H}^0 N^2 H_n H_m\,\mathrm{d}z = f^2 r_n^2 \delta_{m,n}. \tag{3.10}$$

The F_n, G_n and H_n can be used to project the dynamical fields according to

$$(u, v) = \sum_{n=1}^{\infty} (u_n, v_n) F_n, \quad w = \sum_{n=1}^{\infty} w_n H_n, \quad \rho = \sum_{n=1}^{\infty} \rho_n G_n. \tag{3.11}$$

Here u_n, v_n, w_n and ρ_n are functions of x, y and t. Their Fourier transforms with respect to these three independent variables, denoted by a hat, satisfy

$$u_n = \iiint \hat{u}_n(k, l, \omega) \mathrm{e}^{\mathrm{i}(kx+ly-\omega t)}\,\mathrm{d}k\,\mathrm{d}l\,\mathrm{d}\omega \tag{3.12}$$

and similar. Introducing (3.11)–(3.12) into the linearized hydrostatic–Boussinesq equations leads to the dispersion relation

$$\omega^2 = f^2 + f^2 r_n^2 (k^2 + l^2), \tag{3.13}$$

for each mode n with frequency ω and horizontal wavenumbers (k, l). The corresponding polarization relations read

$$\hat{u}_n = \left(\frac{f l}{\omega(k^2 + l^2)} - \mathrm{i} \frac{k}{k^2 + l^2} \right) \hat{w}_n, \tag{3.14a}$$

$$\hat{v}_n = -\left(\frac{f k}{\omega(k^2 + l^2)} + \mathrm{i} \frac{l}{k^2 + l^2} \right) \hat{w}_n, \tag{3.14b}$$

$$\hat{\rho}_n = \mathrm{i} \frac{\rho_0 r_n f}{g\omega} \hat{w}_n. \tag{3.14c}$$

Note that, for a given mode n and horizontal wavenumber (k, l), the energy is concentrated on two opposite frequencies which are solution of (3.13).

Using (3.13) and (3.14), the vertical profile of the energy (3.5) averaged in time becomes

$$\mathscr{E}_z(z) = \frac{\rho_0}{2VT} \sum_n \iiint \left(\frac{\omega^2 + f^2}{\omega^2(k^2 + l^2)} F_n^2(z) + \frac{\omega^2 - f^2}{\omega^2(k^2 + l^2)} \frac{G_n^2(z)}{N^2(z)} \right) |\hat{w}_n|^2\,\mathrm{d}k\,\mathrm{d}l\,\mathrm{d}\omega, \tag{3.15}$$

assuming that the domain size and duration T of the simulation are much larger than the wavelengths and periods of the energy-containing IGWs.

The first and second terms on the right-hand side of (3.15) represent the kinetic and potential energies, respectively. One can integrate this equation over the depth of the domain using the orthogonality relations (3.10), and find the following equation for the

https://doi.org/10.1017/jfm.2012.90 Published online by Cambridge University Press

total energy per volume unit:

$$\mathscr{E} = \int_{-H}^{0} \mathscr{E}_z(z)\,\mathrm{d}z = \frac{\rho_0}{VT} \sum_n \iiint \frac{|\hat{w}_n|^2}{k^2 + l^2}\,\mathrm{d}k\,\mathrm{d}l\,\mathrm{d}\omega. \tag{3.16}$$

This formula is useful to estimate the IGW contribution to the total energy from the unbalanced vertical velocity only.

4. Results

4.1. *Extraction of the wave signal*

We apply the two methods of extraction of the IGW vertical and horizontal velocities described in §§ 3.1 and 3.2 to our numerical simulation and examine the results both in the physical and the frequency–wavenumber domains. We use model data sampled every 1.5 h; this high temporal resolution and the relatively long sample used (120 h) make it possible to resolve frequencies in the range $0.15f$–$6f$.

A typical snapshot of the vertical velocity field at $z = -2500$ m is shown in figure 3: the total field w (figure 3*a*) is compared with the solution w_{qg} of the omega equation (figure 3*b*) and with the unbalanced contribution $w_{unb} = w - w_{qg}$ (figure 3*c*). At this depth, the total vertical velocity appears to be a superposition of a large-scale balanced motion and a small-scale unbalanced motion. Both types of motion have similar amplitudes, with a root-mean-square (r.m.s.) value of $\sim 3 \times 10^{-5}$ m s^{-1}. However, the unbalanced velocity displays much stronger extrema with values reaching 10^{-3} m s^{-1}, while the balanced velocity does not exceed 2×10^{-4} m s^{-1}. The depth of 2500 m is intermediate in our simulation: below 2500 m the unbalanced vertical velocities dominate the balanced ones (the ratio of their r.m.s. tends to 4 close to the bottom), while above 2500 m balanced vertical velocities dominate (the ratio of their r.m.s. is 0.25 at $z = -1000$ m for instance). The comparison of figure 3(*a–c*) highlights the effectiveness of the omega equation as a tool to separate the balanced and unbalanced components of the flow: the balanced w_{qg} is free from traces of the small-scale IGWs, while the unbalanced $w - w_{qg}$ is dominated by IGWs, with only a weak remnant of the large-scale balanced motion.

The overall picture of the unbalanced vertical velocity at 2500 m is one of roughly (horizontally) isotropic interfering waves. The amplitude of these waves is largely homogeneous, with r.m.s. values of 2×10^{-5} m s^{-1} on most of the domain. However, at any one time, a few regions display a much stronger wave activity, characterized by much higher local r.m.s. values (up to 5×10^{-4} m s^{-1}). At the time chosen for figure 3, regions of this type appear for instance around $(x, y) = (210\text{ km}, 1150\text{ km})$ or $(x, y) = (70\text{ km}, 630\text{ km})$. The strong curvature of the crests and troughs in these regions suggest that the waves there have just been emitted. Another interesting region extends from $x = 0$ to 250 km and $y = 700$ to 900 km. The shape of the waves in this region strongly suggest a prior emission around $(x, y) = (80\text{ km}, 450\text{ km})$; this has been verified on plots of the three vertical velocities at earlier times (not shown).

The picture that emerges from the simulation, especially when examining animations of the vertical velocity data, is of a generation of IGWs that is highly intermittent in space and time. After each generation event, the waves emitted propagate, disperse, are refracted and interfere to create a complex time-dependent wave field.

A view of the unbalanced motion complementary to that given by the representation of the field in physical space is provided by power spectra in the horizontal wavenumber–frequency domain. Figure 4 displays several such spectra: (*a–c*) shows the spectra of the vertical velocities w, w_{qg} and $w - w_{qg}$ (figure 4*a–c*); (*d–f*) shows

https://doi.org/10.1017/jfm.2012.90 Published online by Cambridge University Press

the kinetic energy spectra corresponding to the total horizontal velocity, the balanced horizontal velocity obtained by solving (3.7) and the unbalanced horizontal velocity derived by substraction (figure 4*d–f*). These spectra have been obtained at a depth $z = -2500$ m by first calculating the horizontal Fourier transform $\tilde{\phi}(k, l, z, t)$ of each variable $\phi(x, y, z, t)$ (where ϕ is the total, balanced and unbalanced vertical or horizontal velocity), then Fourier-transforming in time to obtain the horizontal wavenumber–frequency transform $\hat{\phi}(k, l, z, \omega)$ and finally summing the values of $|\hat{\phi}(k, l, z, \omega)|^2$ over the wavenumbers (k, l) such that $\sqrt{k^2 + l^2} \in [k_h, k_h + dk_h]$.

The total vertical velocity spectrum (figure 4*a*) displays two distinct energetic regions: the first region is characterized by low frequencies ($\omega \lesssim f/2$) and relatively large scales ($k_h \lesssim 1 \times 10^{-4}$ m^{-1}), while the second region is characterized by high frequencies ($\omega \gtrsim f$) and small scales ($k_h \gtrsim 1 \times 10^{-4}$ m^{-1}). The first region is associated with the balanced motion, as is confirmed by the spectrum of the balanced velocity w_{qg} (figure 4*b*); the second region is associated with the unbalanced motion (figure 4*c*). The power integrated over these two regions in the (ω, k_h) spectrum has been computed and give similar values ($\sim 3 \times 10^{-5}$ m s^{-1}), consistent with the r.m.s. associated with the two types of motion in physical space. Note that although most of the power of the unbalanced vertical velocity in figure 4(*c*) is contained at frequencies higher than f, some remains at lower frequencies because the omega equation provides only a first-order approximation to the balanced velocity. Note also that the balanced velocity spectrum is absolutely depleted of energy in the region ($\omega \gtrsim f, k_h \gtrsim 2 \times 10^{-4}$ m^{-1}): this shows that the omega equation efficiently filters out IGWs.

The dispersion relation for the first few IGW modes, given by $\omega^2 = f^2 + f^2 r_n^2 k_h^2$ (see (3.13)) is also plotted in figure 4. The unbalanced vertical power (figure 4*c*) follows the dispersion curves well, confirming that the unbalanced activity consists mainly of free linear IGWs. A striking feature in the figure is that the vertical-velocity spectrum is almost constant along the dispersion curves; in particular, there is no marked decay as the frequency increases. This provides some information about the spontaneous-generation mechanism which we discuss further in §5.

The horizontal wavenumber–frequency spectra of the horizontal kinetic energy plotted in figure 4(*d–f*) indicate that the inversion (3.7) is less efficient to recover the unbalanced component of the horizontal velocity than the omega equation for the vertical velocity. Figure 4(*f*), in particular, shows only a weak concentration of the energy associated with $\boldsymbol{u} - \boldsymbol{u}_g$ along the dispersion curve. This energy decreases rapidly as frequency and wavenumber increase, unlike the vertical-velocity spectrum in figure 4(*c*); this is consistent with the polarization relations (3.14), which predicts a decrease of the kinetic energy $|\hat{u}_n|^2 + |\hat{v}_n|^2$ in k_h^{-2} as frequency and wavenumber increase for a constant $|\hat{w}_n|^2$. In any case, most of the energy associated with $\boldsymbol{u} - \boldsymbol{u}_g$ is at frequencies lower than f and large scales, indicating that the inversion method (3.7) is not sufficiently accurate to separate IGWs from the balanced part of the flow. The omega equation performs substantially better, unsurprisingly since its error is $O(Ro^2)$ while that of the inversion (3.7) is only $O(Ro)$.

4.2. *IGW energy*

Even though the amplitudes of IGWs excited by spontaneous generation are very small, it is of interest to estimate the energy $\mathscr{E}$ and vertical flux of energy $\overline{p_{unb} w_{unb}}$ for the IGW field in our simulation. Owing to the limitations of the inversion (3.7) for the small wave amplitudes we have to deal with, it is not possible to obtain a reliable

https://doi.org/10.1017/jfm.2012.90 Published online by Cambridge University Press

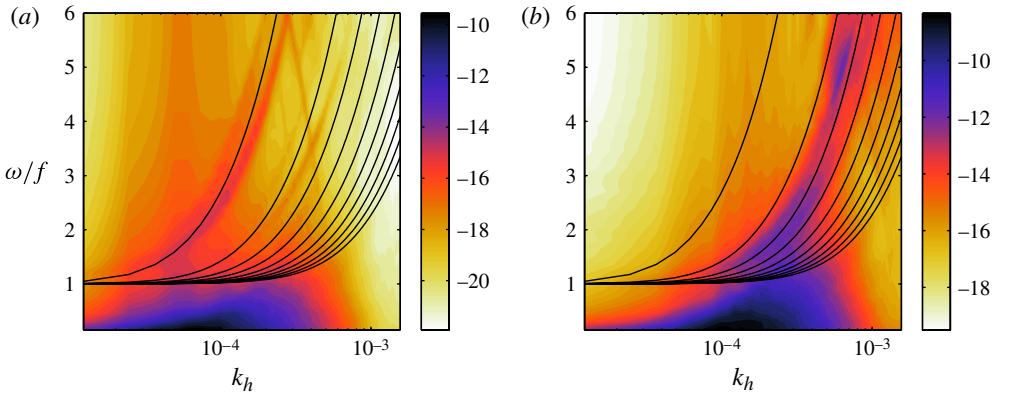


FIGURE 5. (Colour online) Frequency–horizontal wavenumber spectrum (log-scale) of the first (*a*) and third (*b*) modes of the vertical velocity. The dispersion relation $\omega^2 = f^2 + f^2 r_d^2 k_h^2$ for the first 10 vertical modes is represented by the black curves. Note that the apparent reflection at the intersection of the dispersion curve for $n = 1$ with the upper boundary of (*a*) results from an aliasing effect that could be eliminated by improved sampling.

estimate of the vertical energy flux. We therefore concentrate on the energy itself and use (3.15) and (3.16) to infer the vertical profile of the IGW energy density $\mathscr{E}_z$ and total IGW energy $\mathscr{E}$ from w_{unb} approximated as $w - w_{qg}$.

A first step is to compute the horizontal wavenumber–frequency spectrum of each mode n. Figure 5(*a*,*b*) display the spectra of modes 1 and 3, respectively. Both spectra clearly show a concentration of energy along the dispersion relation of the mode considered, with an almost-constant amplitude as figure 4(*e*) already suggested. (Note that some mode 1 energy is localized near the dispersion relation of mode 2; this is unsurprising since the hypothesis of free linear IGWs propagating in a fluid at rest is not satisfied exactly.) The energy at $\omega \lesssim f$ apparent in figure 5(*a*,*b*) is associated with the part of the balanced velocity not resolved by the omega equation and cannot be attributed to IGW motion. Note that this effect is much stronger when separate vertical modes are considered than for the full vertical velocity at $z = -2500$ m (see figure 4*e*); this is because the calculation of a component n according to

$$w_n = \frac{1}{f^2 r_n^2} \int_{-H}^{0} N^2 (w_{unb} + O(Ro^2)) H_n \, \mathrm{d}z \tag{4.1}$$

involves an integral over the whole depth of the domain, including surface regions where the $O(Ro^2)$ error terms are important (since Ro can be large locally) and where N^2 is large. (Typical profiles of the functions H_n can be found in figure 1*c* in Danioux *et al.* (2008).) In order to estimate the IGW energy as accurately as possible, we have therefore restricted the domains of integration in (3.15) and (3.16) to regions around the dispersion relation of each mode: for example, for mode 3, the energy located beyond the dispersion relations of neighbouring modes 2 and 4 is removed.

The vertical profile of energy $\mathscr{E}_z$ is plotted in figure 6(*a*), where we restricted our calculation to the first 20 vertical modes (thick black line). The figure also displays the cumulative contribution of the first 5, 10 and 15 modes and shows that most of the energy is contained in modes 1–10, with a substantial contribution of relatively high modes ($5 < n \leqslant 10$). Also represented in figure 6(*b*) is the energy profile associated with the IGWs of frequency higher than $2f$; as expected, for these

https://doi.org/10.1017/jfm.2012.90 Published online by Cambridge University Press

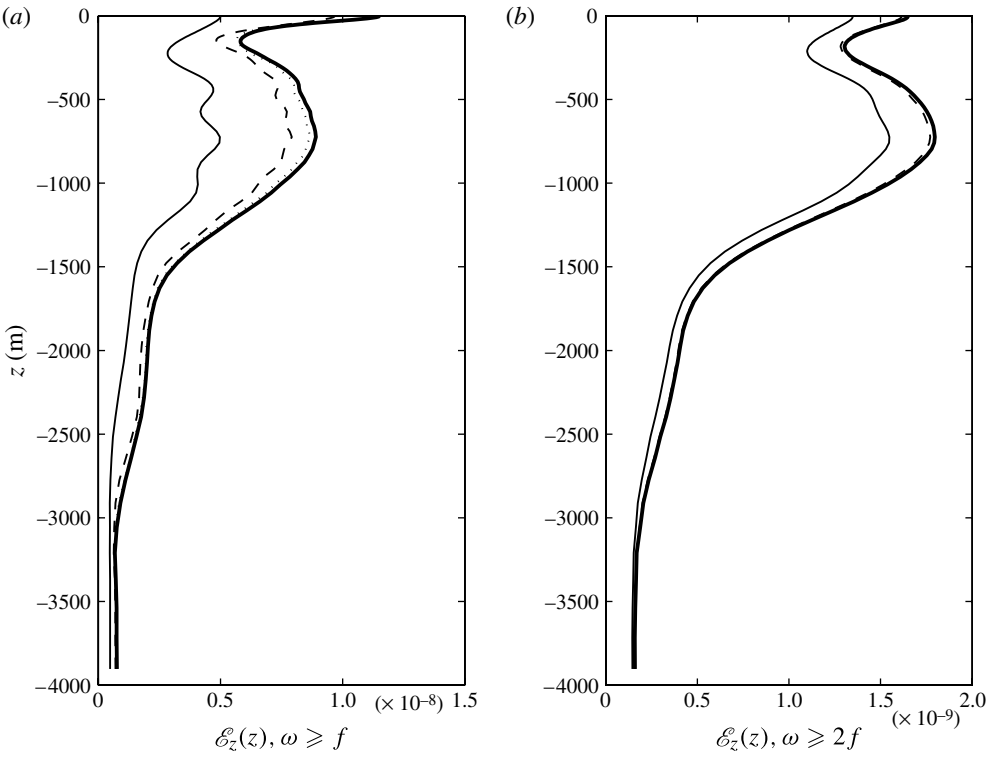


FIGURE 6. Vertical density of the IGW energy: the contributions of the first 5 (thin solid line), 10 (dashed line), 15 (dotted line) or 20 (thick solid line) vertical modes are shown for frequencies higher than f (a) or $2f$ (b). The profiles are averaged over the duration of the simulation (see (3.15)). Note the different scales in (a,b).

waves, the convergence is faster with more than 98 % of the energy being in modes $\leqslant 10$. The energy profile of figure 6(a) displays similarities with the profile of N shown in figure 1. This can be understood in the context of the geometric–optics (or WKB) approximation, which applies strictly to high modes only but qualitatively to all but the gravest modes $n = 1, 2, 3$. In this approximation and ignoring Doppler-shift effects, the dispersion relation

$$\omega^2 = f^2 + N^2 \frac{k^2 + l^2}{m^2}, \tag{4.2}$$

where m is the (local) vertical wavenumber, applies (e.g. Gill 1982, chap. 8), and the energy density, $\mathscr{E}_{xyz}$ say, is conserved:

$$\frac{\partial \mathscr{E}_{xyz}}{\partial t} + \boldsymbol{\nabla} \cdot (\mathbf{c}_g \mathscr{E}_{xyz}) = 0, \tag{4.3}$$

where $\mathbf{c}_g = (c_{gx}, c_{gy}, c_{gz})$ is the group velocity (e.g. Bühler 2009, p. 83). Averaging over time and the horizontal coordinates, this reduces to

$$\frac{\partial}{\partial z}(\mathscr{E}_z c_{gz}) = 0. \tag{4.4}$$

https://doi.org/10.1017/jfm.2012.90 Published online by Cambridge University Press

Since, according to (4.2),

$$c_{gz} = \frac{\partial \omega}{\partial m} = \pm \frac{(\omega^2 - f^2)^{3/2}}{\omega k} \times \frac{1}{N(z)}, \tag{4.5}$$

where the first factor is independent of z, it follows that $\mathscr{E}_z \propto N(z)$ for high modes.

Integrating the profile $\mathscr{E}_z$ in figure 6 over the depth of the domain, we find the average energy per volume unit of the IGWs generated spontaneously in our simulation to be $\mathscr{E} = 1 \times 10^{-5}$ J m^{-3}. To put this into perspective, we can compare this result with the energy of the oceanic IGW field as described by the empirical Garrett–Munk spectrum. This yields the much larger estimate of $\mathscr{E} = 1$ J m^{-3} (e.g. Thorpe 2005). Thus, the source of IGWs provided by spontaneous generation appears to be orders of magnitude weaker than the main sources namely generation by wind and by tides and their interactions with topography. Although the energy of IGWs in our simulation is probably diminished by the artificially large dissipation of the numerical model, this conclusion is certainly robust; it is also confirmed by comparison with the energy of wind-generated inertial waves in a model with similar configuration (compare figure 3 with figure 1*d* in Danioux *et al.* (2011)).

It should be remarked that the hydrostatic approximation, employed for the numerical model as well as for the analysis leading to (3.13) and (4.2) and which assumes IGW frequencies significantly smaller than N, is invalidated near the bottom where $N \approx f$. The approximation is however well justified near the surface where the spontaneous emission occurs. In addition, it holds for waves with frequencies $\omega \lesssim 2f$, which contain most of the energy (see figure 6), for depth down to 3500 m so that the vertical propagation process is also largely described faithfully.

4.3. *Generation and evolution of a wavepacket*

In this section, we examine the generation and early stage of development of a specific IGW packet. It is typically difficult to extract information on the structure of IGWs, as the motion at a given point is the sum of different wavepackets generated at different times/places which have propagated. However, immediately after the generation of a wavepacket, the associated vertical velocities are sufficiently large that they dominate the background of interfering waves. Thus, the sites and times of generation can be identified easily by large values of the local r.m.s. of w. In figure 3(*c*), for example, the region around $(x, y) = (210 \text{ km}, 1150 \text{ km})$ is such a generation site.

Figure 7 focuses on the generation of a particular wavepacket by juxtaposing plots of the unbalanced vertical velocity at $z = -2500$ m and every 12 h with the corresponding plots of the surface relative vorticity. The vertical velocity plots (*a*,*c*,*e*,*g*) clearly show the generation of an IGW wavepacket which emerges from the background field. Its amplitude gradually increases until it reaches values $\sim$10 times larger than the background values in figure 7(*g*). In the subsequent evolution (not shown), the wavepacket propagates and disperses, and its amplitude decreases slowly to the background value. The generation of the wavepacket coincides in time and space with the appearance of a strong relative vorticity filament at the surface (figure 7*b*,*d*,*f*,*h*), with values of vorticity reaching 3×10^{-4} s^{-1}. The increase in vorticity results from the straining of a filament of surface density, a process well understood in the SQG approximation (e.g. Held *et al.* 1995). A significant feature in the evolution of the vorticity is that it is more complex than the simple straining of a front or even a straight filament, with filament curvature and displacement of the vorticity maximum expected to play a role in the process of spontaneous generation. The spatial scale

https://doi.org/10.1017/jfm.2012.90 Published online by Cambridge University Press

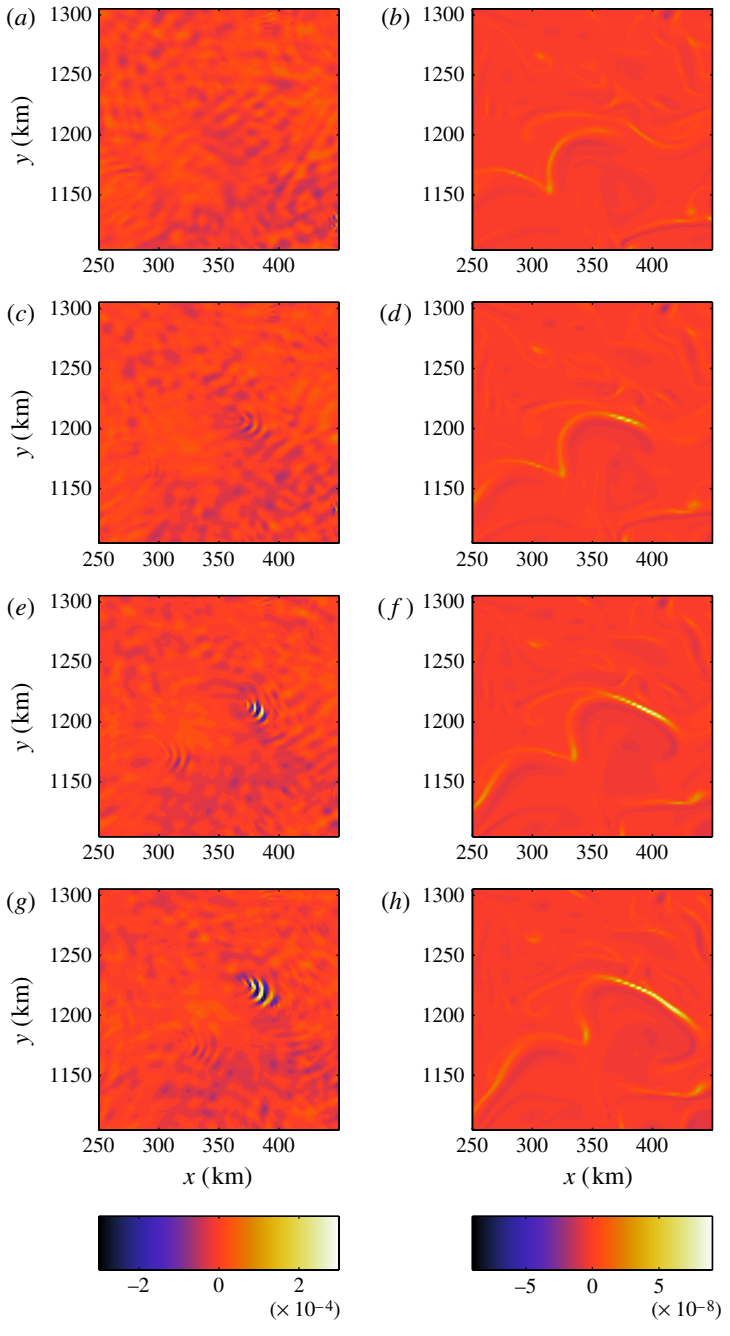


FIGURE 7. (Colour online) Generation of a wavepacket by a vorticity filament: (*a*,*c*,*e*,*g*) unbalanced vertical velocity w_{unb} at $z = -2500$ m; (*b*,*d*,*f*,*h*) $\mathrm{sign}(\zeta) \cdot \zeta^2$, where ζ is the surface relative vorticity, at different instants separated by 12 (*c*,*d*), 24 (*e*,*f*) and 36 (*g*,*h*) hours from (*a*,*b*).

of both the filament and the wavepacket that emanates from it is quite close to the model resolution but these features are nonetheless well resolved, and we expect they

https://doi.org/10.1017/jfm.2012.90 Published online by Cambridge University Press

would remain mostly unchanged in simulations with higher resolution but the same level of dissipation. The situation might be different for higher-resolution simulations with significantly lower dissipation, however; we comment further on this point in § 5.

We have checked in our simulation that the generation scenario just described is typical of all wavepacket generation events observed. This demonstrates that spontaneous IGW generation is intimately linked to the dynamics of the surface: more precisely, the generation sites are associated with strong stretching events, which lead to large values of the surface relative vorticity, with the local Rossby number reaching values of 3–4. Below these values, little or no wavepacket generation appears to happen. The strong sensitivity to the local Rossby number is consistent with theoretical models predicting IGW amplitudes depending exponentially on Ro^{-1} (Vanneste & Yavneh 2004; Ólafsdóttir *et al.* 2008; Vanneste 2008*b*). As a result, spontaneous generation is a highly localized and intermittent source of IGW activity.

A more detailed picture of the propagation of wavepackets is provided by the vertical structure of the unbalanced vertical velocity. Although the omega equation best extracts the unbalanced vertical velocity at depth (because of a better ratio of unbalanced to balanced vertical velocities), it is sometimes possible to identify the waves up to the surface during or immediately after a generation event thanks to their comparatively strong amplitude. Figure 8 displays vertical (*a*i–*a*iv) and horizontal sections (*b*i–*b*iv in subsurface; *c*i–*c*iv at depth) of the unbalanced vertical velocity during and after the generation of a wavepacket at four instants separated by 7.5 h intervals. The phase lines associated with the wavepacket are identified by the alternating stripes. The large amplitude patches of approximately 10 km scale concentrated near the surface in the (*a*i)–(*a*iv) and (*b*i)–(*b*iv) are submesoscale features poorly filtered out by our method of extraction of the unbalanced signal: recall that what is represented here is the sum of the IGW vertical velocity plus a balanced residual of order $O(Ro^2)$ (see § 3.1): at surface this residual can become large.

Figure 8 indicates northward propagation (i.e. to right on the figure) of the wavepacket energy, corresponding to a group velocity $c_g = (c_{gx}, c_{gy}, c_{gz})$ with $c_{gy} > 0$. This, along with the slope of the phase lines, indicates downward propagation of the wave energy, that is, $c_{gz} < 0$ (e.g. Gill 1982). This is consistent with our interpretation as IGWs spontaneously generated by dynamics near the surface. This is also confirmed by the fact that the wavepacket appears at $z = -200$ m before $z = -2500$ m (compare figure 8*b*i,*c*i, and later on *b*ii,*c*ii). The phase and group velocity vectors are indicated in figure 8(*a*ii). Values for the horizontal and vertical wavenumbers near the thermocline are $l = 8 \times 10^{-4}$ m^{-1} and $m = 1.2 \times 10^{-2}$ m^{-1}, respectively.

Another feature of the wavepacket is the decrease of the vertical wavenumber with depth, reaching a near-zero value between $z = -2000$ m and $z = -4000$ m. This can be understood using the geometric–optics approach for wavepackets in a variable medium (e.g. Bühler 2009, p. 74). At short times after the wavepacket generation, advection by the balanced flow can be neglected, so that the horizontal wavenumber remains constant following the wavepacket. This can be verified from figure 8 which shows that the horizontal wavenumber in the subsurface is approximately the same as at depth. This property, along with the conservation of the frequency ω in (4.2), implies that the ratio N m^{-1} is kept constant as the wavepacket propagates downwards. This argument predicts a vertical wavenumber at $z = -3000$ m

$$m(-3000\ \text{m}) = \frac{N(-3000\ \text{m})}{N(-600\ \text{m})} \times m(-600\ \text{m}) \simeq 1.9 \times 10^{-3}\ \text{m}^{-1}, \tag{4.6}$$

https://doi.org/10.1017/jfm.2012.90 Published online by Cambridge University Press

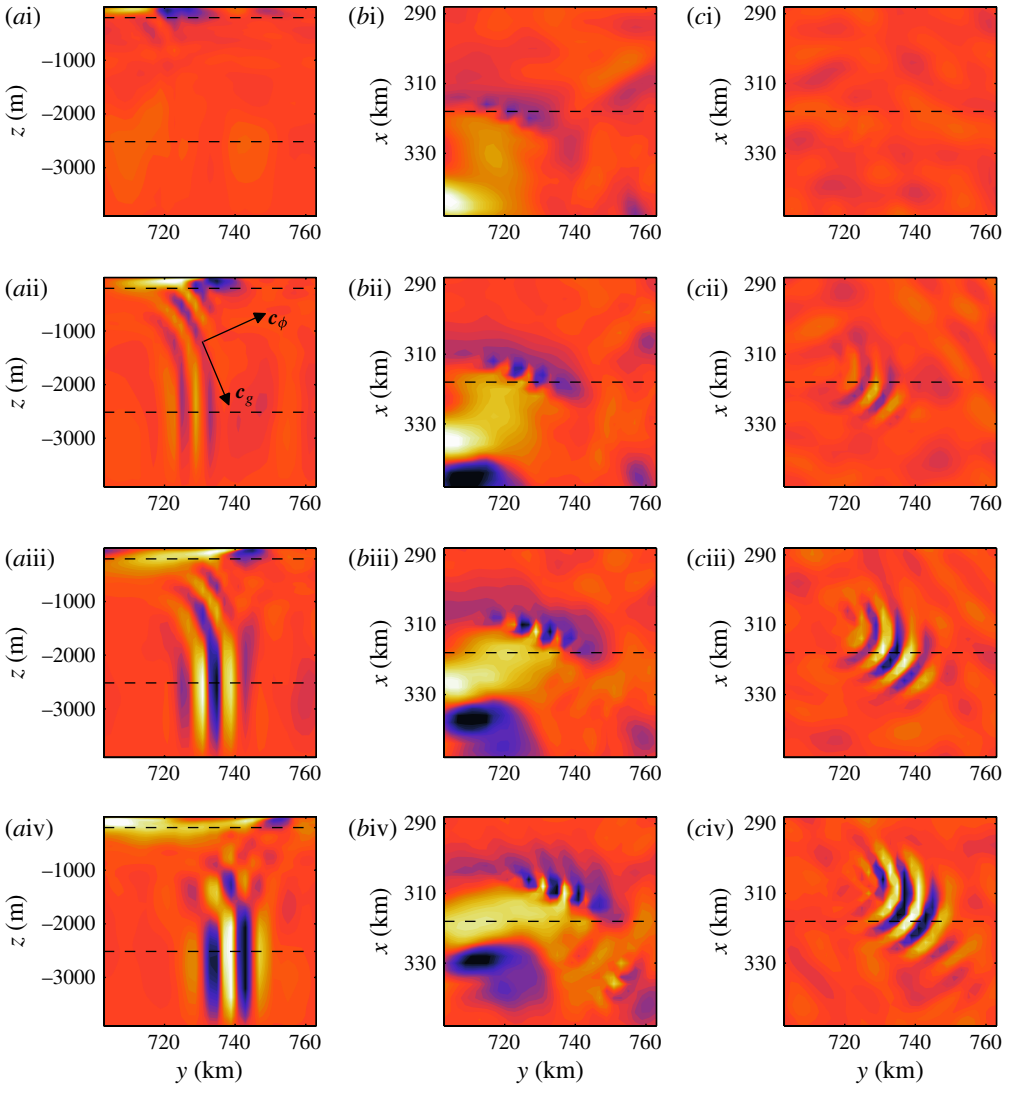


FIGURE 8. (Colour online) Time evolution of a wavepacket. The difference between the total and quasi-geostrophic vertical velocities $w - w_{qg} = w_{unb} + 0(Ro^2)$ is shown in vertical (left column) and horizontal (middle and right columns) cross-sections at different instants separated by 7.5 (*a*ii,*b*ii,*c*ii), 15 (*a*iii,*b*iii,*c*iii) and 22.5 (*a*iv,*b*iv,*c*iv) hours from (*a*i), (*b*i) and (*c*i). The horizontal cross-sections correspond to $z = -200$ m (middle column) and -2500 m (right column). These sections are indicated on (*a*i–*a*iv) by the dashed lines. The vertical cross-section corresponds to $x = 318$ km, as indicated by the dashed line in (*b*i–*b*iv) and (*c*i–*c*iv). The colourbar extends from -4 to 4×10^{-4} m s^{-1}. Note that absolute values beyond the range of the colourbar may occur locally: (*a*i) $w(318\text{ km}, y, z, t)$; (*b*i) $w(x, y, -200\text{ m}, t)$; (*c*i) $w(x, y, -2500\text{ m}, t)$; (*a*ii) $w(318\text{ km}, y, z, t + 7.5\text{ h})$; (*b*ii) $w(x, y, -200\text{ m}, t + 7.5\text{ h})$; (*c*ii) $w(x, y, -2500\text{ m}, t + 7.5\text{ h})$; (*a*iii) $w(318\text{ km}, y, z, t + 15\text{ h})$; (*b*iii) $w(x, y, -200\text{ m}, t + 15\text{ h})$; (*c*iii) $w(x, y, -2500\text{ m}, t + 15\text{ h})$; (*a*iv) $w(318\text{ km}, y, z, t + 22.5\text{ h})$; (*b*iv) $w(x, y, -200\text{ m}, t + 22.5\text{ h})$; (*c*iv) $w(x, y, -2500\text{ m}, t + 22.5\text{ h})$.

which corresponds to a wavelength of the order of the depth of the domain, hence the almost vertically homogeneous waves in depth as observed. Note that a slight

https://doi.org/10.1017/jfm.2012.90 Published online by Cambridge University Press

reflection on the bottom surface is visible in figure 8(*a*iv) in the form of phase lines with slope opposite to that of the main wavepacket.

At large times, the advection by the balanced flow cannot be neglected: the wavepacket propagates and is deflected by the flow. The wavenumber can change as a result of advection, explaining why, as observed in figure 4(*e*), there is a broad range of horizontal scales in the IGW field, while the scales at generation are rarely larger than 5–10 km.

5. Discussion

The analysis reported in this paper demonstrates that the evolution of near-surface turbulence, which at large scales at least is well modelled by the SQG theory, is accompanied by the emission of IGWs propagating into the fluid interior. This emission is an example of spontaneous generation of IGWs by time-dependent balanced flows, a phenomenon that is generic to all flows described by the primitive equations. What makes surface motion particulary interesting, however, is that the associated scale cascade leads naturally to large Rossby number at small scales (Juckes 1994) and, as a result, to increased IGW generation. Because this generation occurs at small scales, their simulation in a flow that is forced at large scales only requires a very high resolution.

In the simulation described here, IGW generation is found to be highly localized in space and time. This is consistent with the exponential dependence in the Rossby number that is predicted for idealized models using asymptotic methods (Vanneste 2008*b*, and references therein): the exponential dependence is extremely sharp and implies that a relatively smooth spatial distribution of local Rossby number corresponds to highly intermittent wave generation. The small-Rossby-number asymptotic results are only indicative, however, since the IGW generation events identified in the simulation take place in regions where the Rossby number is well above 1. It is in fact difficult to see how wave generation in this regime can be analysed by means other than direct simulations: at the generation sites, there is no separation of either time or spatial scales between balanced and unbalanced motions.

Nonetheless, because the balanced motion is localized near the surface, the Rossby numbers are small in the fluid's interior, and the separation between balanced and unbalanced motions is well justified there. This is why we are able to isolate IGWs successfully at depth using nothing more sophisticated than the quasi-geostrophic relations to approximate the balanced motion. One of the interesting features that emerge from the analysis is that the IGW vertical-velocity spectrum is approximately constant along the branches of the IGW dispersion relation in the (k_h, ω)-plane. This corresponds to a total IGW energy that decays like k_h^{-2} or, equivalently, like $(\omega^2 - f^2)^{-1}$. It is tempting to relate the k_h^{-2} behaviour to the energy spectrum $E(k) \sim k_h^{-2}$ of SQG-like turbulence, but this may be misleading since the strength of the balanced motion as a source of IGWs is unlikely to depend specifically on the balanced-motion energy. For example, it may be argued that it is the matching between the frequencies of the balanced motion and those of gravity waves that matters; in this case, the frequency spectrum of the balanced motion $\tilde{E}(\omega) = E(k_h)\,\mathrm{d}k_h/\mathrm{d}\omega$ is relevant. Arguments based on WKB theory in fact suggest that the Lagrangian frequency spectrum should be considered (Aspden & Vanneste 2010).

The amplitudes of the IGWs generated spontaneously in the simulation analysed here are very small when compared with typical amplitudes of oceanic IGWs: indeed, their energy is found to be smaller by a factor of $\sim 10^5$ than the energy inferred

https://doi.org/10.1017/jfm.2012.90 Published online by Cambridge University Press

from the Garrett–Munk spectrum. It can be argued that the limited resolution of the numerical model reduces substantially the efficiency of spontaneous generation. In SQG-like turbulence, frequencies increase as spatial scales decrease, so that the Rossby numbers, and hence presumably IGW generation, are the largest at the smallest scales. Submesoscale instabilities as described in Capet *et al.* (2008*b*), which are smoothed in our simulation, are also likely to play a significant role for spontaneous generation. However, in view of the comparatively much larger amplitudes of IGWs generated by other processes (wind, tides), we have to conclude that spontaneous generation is unlikely to be a significant contributor to the total IGW energy in the ocean. A similar conclusion cannot be drawn for the atmosphere, however, simply because there are in this case no clear alternative sources of non-stationary IGWs.

Acknowledgement

This research was supported by grant NE/F002807/1 of the UK Natural Environment Research Council.

REFERENCES

ADAMS, J. 1989 Mudpack: multigrid Fortran software for the efficient solution of linear elliptic partial differential equations. *Appl. Maths Comput.* **34**, 113–146.

ASPDEN, J. M. & VANNESTE, J. 2010 Inertia-gravity-wave generation: a geometric–optic approach. In *IUTAM Symposium on Turbulence in the Atmosphere and Oceans* (ed. D. Dritschel), Springer.

BENDER, C. M. & ORSZAG, S. A. 1999 *Advanced Mathematical Methods for Scientists and Engineers*. Springer.

BLUMEN, W. 1978 Uniform potential vorticity flow. Part I: theory of wave interactions and two-dimensional turbulence. *J. Atmos. Sci.* **35**, 421–432.

BÜHLER, O. 2009 *Waves and Mean Flows*. Cambridge University Press.

CAPET, X., MCWILLIAMS, J. C., MOLEMAKER, M. J. & SHCHEPETKIN, A. F. 2008*a* Mesoscale to submesoscale transition in the California current system. Part I: flow structure, eddy flux, and observational tests. *J. Phys. Oceanogr.* **38**, 29–43.

CAPET, X., MCWILLIAMS, J. C., MOLEMAKER, M. J. & SHCHEPETKIN, A. F. 2008*b* Mesoscale to submesoscale transition in the California current system. Part II: frontal processes. *J. Phys. Oceanogr.* **38**, 44–64.

CAPET, X., MCWILLIAMS, J. C., MOLEMAKER, M. J. & SHCHEPETKIN, A. F. 2008*c* Mesoscale to submesoscale transition in the California current system. Part III: energy balance and flux. *J. Phys. Oceanogr.* **38**, 2256–2269.

DANIOUX, E. & KLEIN, P. 2008 A resonance mechanism leading to wind-forced motions with a $2f$ frequency. *J. Phys. Oceanogr.* **38**, 2322–2329.

DANIOUX, E., KLEIN, P., HECHT, M., KOMORI, N., ROULLET, G. & GENTIL, S. L. 2011 Emergence of wind-driven near-inertial waves in the deep ocean triggered by small-scale eddy vorticity structures. *J. Phys. Oceanogr.* **41**, 1297–1307.

DANIOUX, E., KLEIN, P. & RIVIÈRE, P. 2008 Propagation of wind energy into the deep ocean through a fully turbulent mesoscale eddy field. *J. Phys. Oceanogr.* **38**, 2224–2241.

GILL, A. 1982 *Atmosphere Ocean Dynamics*. Academic.

GRIFFITHS, M. & REEDER, M. J. 1996 Stratospheric inertia-gravity waves generated in a numerical model of frontogenesis. I: Model solutions. *Q. J. R. Meteorol. Soc.* **122**, 1153–1174.

HELD, I., PIERREHUMBERT, R., GARNER, S. & SWANSON, K. 1995 Surface quasi-geostrophic dynamics. *J. Fluid Mech.* **282**, 1–20.

HOSKINS, B. J. & BRETHERTON, F. P. 1972 Atmospheric frontogenesis models: mathematical formulation and solutions. *J. Atmos. Sci.* **29**, 11–37.

HOSKINS, B., DRAGHICI, I. & DAVIES, H. 1978 A new look at the ω-equation. *Q. J. R. Meteorol. Soc.* **104**, 31–38.

https://doi.org/10.1017/jfm.2012.90 Published online by Cambridge University Press

JUCKES, M. 1994 Quasi-geostrophic dynamics of the tropopause. *J. Atmos. Sci.* **51**, 2756–2768.

KARSTEN, R., JONES, H. & MARSHALL, J. 2002 The role of eddy transfer in setting the stratification and transport of a circumpolar current. *J. Phys. Oceanogr.* **32**, 39–54.

KLEIN, P., HUA, B., LAPEYRE, G., CAPET, X., GENTIL, S. L. & SASAKI, H. 2008 Upper ocean turbulence from high-resolution 3D simulations. *J. Phys. Oceanogr.* **38**, 1748–1763.

KRAICHNAN, R. H. 1971 Inertial-range transfer in two- and three-dimensional turbulence. *J. Fluid Mech.* **47**, 525–535.

LAPEYRE, G. & KLEIN, P. 2006 Dynamics of the upper oceanic layers in terms of surface quasigeostrophy theory. *J. Phys. Oceanogr.* **36**, 165–176.

LARGE, W., DONEY, S. & MCWILLIAMS, J. 1994 Oceanic vertical mixing: a review and a model with a non-local boundary layer parameterization. *Rev. Geophys.* **31**, 363–403.

MCWILLIAMS, J. C., MOLEMAKER, M. J. & ÓLAFSDÓTTIR, E. I. 2009 Linear fluctuation growth during frontogenesis. *J. Phys. Oceanogr.* **39**, 3111–3129.

MOLEMAKER, M. J., MCWILLIAMS, J. C. & CAPET, X. 2010 Balanced and unbalanced routes to dissipation in an equilibrated eady flow. *J. Fluid Mech.* **654**, 35–63.

MURAKI, D. J., SNYDER, C. & ROTUNNO, R. 1999 The next order corrections to quasigeostrophic theory. *J. Atmos. Sci.* **56**, 1547–1560.

NAGAI, T., TANDON, A. & RUDNICK, D. 2006 Two-dimensional ageostrophic secondary circulation at ocean fronts due to vertical mixing and large-scale deformation. *J. Geophys. Res.* **111**, C09038.

ÓLAFSDÓTTIR, E. I., OLDE DAALHUIS, A. B. & VANNESTE, J. 2008 Inertia-gravity-wave radiation by a sheared vortex. *J. Fluid Mech.* **596**, 169–189.

O'SULLIVAN, D. & DUNKERTON, T. J. 1995 Generation of inertia-gravity waves in a simulated life-cycle of baroclinic instability. *J. Atmos. Sci.* **52**, 3695–3716.

PLOUGONVEN, R. & SNYDER, C. 2005 Gravity waves excited by jets: propagation versus generation. *Geophys. Res. Lett.* **32**, L18802.

PLOUGONVEN, R. & SNYDER, C. 2007 Inertia-gravity waves spontaneously excited by jets and fronts. Part I: different baroclinic life cycles. *J. Atmos. Sci.* **64**, 2502–2520.

REEDER, M. J. & GRIFFITHS, M. 1996 Stratospheric inertia-gravity waves generated in a numerical model of frontogenesis. Part II: wave sources, generation mechanisms and momentum fluxes. *Q. J. R. Meteorol. Soc.* **122**, 1175–1195.

RIVIÈRE, P., TRÉGUIER, A.-M. & KLEIN, P. 2004 Effects of bottom friction on nonlinear equilibration of an oceanic baroclinic jet. *J. Phys. Oceanogr.* **34**, 416–432.

SHCHEPETKIN, A. & MCWILLIAMS, J. 2005 The Regional Oceanic Modeling System (ROMS): a split-explicit, free-surface, topography-following coordinate ocean model. *Ocean Model.* **9**, 347–404.

SNYDER, C., MURAKI, D., PLOUGONVEN, R. & ZHANG, F. 2007 Inertia-gravity waves generated within a dipole vortex. *J. Atmos. Sci.* **64**, 4417–4431.

SNYDER, C., SKAMAROCK, W. & ROTUNNO, R. 1993 Frontal dynamics near and following frontal collapse. *J. Atmos. Sci.* **50**, 3194–3211.

TEMAM, R. & WIROSOETISNO, D. 2011 Slow manifolds and invariant sets of the primitive equations. *J. Atmos. Sci.* **68**, 675–682.

THORPE, S. A. 2005 *The Turbulent Ocean*. Cambridge University Press.

VANNESTE, J. 2008*a* Asymptotics of a slow manifold. *SIAM J. Appl. Dyn. Syst.* **7**, 1163–1190.

VANNESTE, J. 2008*b* Exponential smallness of inertia-gravity-wave generation at small Rossby number. *J. Atmos. Sci.* **65**, 1622–1637.

VANNESTE, J. & YAVNEH, I. 2004 Exponentially small inertia-gravity waves and the breakdown of quasi-geostrophic balance. *J. Atmos. Sci.* **61**, 211–223.

VIUDEZ, A. & DRITSCHEL, D. G. 2006 Spontaneous emission of inertia-gravity wave packets by balanced geophysical flows. *J. Fluid Mech.* **553**, 107–117.

WARN, T., BOKHOVE, O., SHEPHERD, T. G. & VALLIS, G. K. 1995 Rossby number expansions, slaving principles, and balance dynamics. *Q. J. R. Meteorol. Soc.* **121**, 723–739.

WILLIAMS, R. T. 1967 Atmospheric frontogenesis: a numerical experiment. *J. Atmos. Sci.* **24**, 627–641.

ZHANG, F. 2004 Generation of mesoscale gravity waves in upper-tropospheric jet-front systems. *J. Atmos. Sci.* **61**, 440–457.

https://doi.org/10.1017/jfm.2012.90 Published online by Cambridge University Press